Evidence of ytterbium doping in $Yb_xZn_{1-x}O$ nanoparticles synthesized by polymer precursor method

M. S. L. Trindade[1], T. S. Silva[1], W. L. R. Pires[1], T. J. Castro[1]*
[1]Instituto Federal de Educação, Ciência e Tecnologia de Brasília, 72146-000, Brasília, DF, Brazil

Abstract

In this work, we report the synthesis of $Yb_xZn_{1-x}O$ nanoparticles ($0.000 \leq x \leq 0.100$) by polymer precursor method and the study of their vibrational and structural properties. Thermal analysis of the polymeric precursor showed that the thermal decomposition occurs in few stages, with the crystallization of the wurtzite structure taking place at a temperature below 500 °C. Fourier transform infrared spectroscopy indicated the presence of Zn-O and Yb-O bonds. X-ray diffraction data showed the formation of the ZnO wurtzite phase for all samples. The application of the Rietveld method revealed a decrease in the average particle size and an increasing trend in unit cell volume as the Yb^{3+} content increased. Additionally, the nearest-neighbor bond lengths along and off the c-direction, as well as the bond angles, were calculated. The results obtained provided additional evidence on the efficiency of Yb^{3+} doping by the polymer precursor method.
Keywords: Yb-doped ZnO, nanoparticles, Rietveld method, polymer precursor method.

INTRODUCTION

The scientific and technological interest in zinc oxide (ZnO) has increased enormously in the last decades due to its exceptional physical properties, especially its wide direct band gap of ~3.37 eV and its large exciton binding energy of ~60 meV at room temperature [1]. In addition, nanomaterials based on rare-earth (RE) doped zinc oxide offer new possibilities for applications, particularly in spintronics and optoelectronics [2]. Regarding rare-earth ions, their high magnetic moment can potentially be used in the search for room temperature ferromagnetism in doped wide band gap semiconductors. On the other hand, 4f-4f transitions in RE ions can give rise to narrow and intense emission lines that are essential in optoelectronics [3]. Furthermore, it has been demonstrated that RE-doped ZnO can present processes of up-conversion (UC) and down-conversion (DC), which can, for example, enhance the efficiency of photovoltaic devices by converting near-infrared or ultraviolet radiation into visible light [4, 5]. For these purposes, ytterbium (Yb) doped zinc oxide nanomaterials are particularly interesting due to the perfect match between their emission band of λ=980 nm and the silicon bandgap [5-7]. Additionally, the combination of Yb^{3+} with other rare-earths, such as Tm^{3+} [8], Ho^{3+} [9], Ce^{3+} [10], and especially Er^{3+} [11-13] can improve the desirable properties for UC applications. Other uses of Yb^{3+}-doped ZnO include dosimetry [6], photocatalysis [14], chemical imaging for clinical diagnosis [15], and chemical sensors [16].

Despite the potential of RE-doped ZnO, it is well known that rare-earths present a low solubility limit in this oxide [17]. This limitation results in a weak energy transfer from the host to rare earths [18], which has a negative impact on the efficiency of technological devices. The low solubility is mainly because, to incorporate RE trivalent ions, the ZnO host needs to undergo significant lattice distortions [19]. In order to produce successful Yb^{3+} doping in ZnO nanomaterials, many experimental techniques have been used such as magnetron reactive sputtering [3], spray pyrolysis [5], atomic layer deposition [7], hydrothermal synthesis [14], co-precipitation method [20], etc. A promising alternative for producing Yb^{3+}-doped ZnO nanopowders is the polymer precursor route, also known as Pechini's method. This technique employs low-cost reagents, does not use complicated steps, can be applied on a large scale, and allows good control of the incorporation of ions and particle size [21]. However, the synthesis of Yb^{3+}-doped ZnO nanoparticles through this method has not been sufficiently explored in the literature, especially for a wider range of Yb^{3+} doping ($0.000 \leq x \leq 0.100$). Therefore, in this study, we report the synthesis and the structural investigation of Yb^{3+}-doped ZnO nanoparticles ($Yb_xZn_{1-x}O$ NPs) with $0.000 \leq x \leq 0.100$. In particular, we highlight the use of the Rietveld method to show the effectiveness of polymer precursor synthesis for the incorporation of ytterbium ions into the host zinc oxide matrix. For this, we explore a more complete approach based on the calculation of the lengths and angles of the chemical bonds.

MATERIALS AND METHODS

$Yb_xZn_{1-x}O$ nanoparticles (NPs with x in the range $0.000 \leq x \leq 0.100$) were synthesized by polymer precursor method using the following reagents: zinc nitrate hexahydrate $[Zn(NO_3)_2.6H_2O]$, ytterbium (III) nitrate pentahydrate $[Yb(NO_3)_3.5H_2O]$, ethylene glycol $[C_2H_4(OH)_2]$, and citric acid $(C_6H_8O_7)$. These materials were purchased from Sigma-Aldrich and were used without further purification.

*tiago.castro@ifb.edu.br
https://orcid.org/0000-0002-9724-3214

As the first step in the synthesis process, the polymeric precursor (resin) was produced. For this purpose, citric acid (47.7 wt%) and zinc nitrate hexahydrate (31.7 wt%) were dissolved in ethylene glycol (20.6 wt%) under magnetic stirring (at ~70 °C). After complete dissolution, when a small amount (~20 mL) of deionized water (D-H$_2$O) was added, the temperature was raised to 120 °C in order to promote the polymerization between citric acid and ethylene glycol. After cooling to room temperature, a yellowish/transparent viscous resin was obtained (Fig. 1). To obtain the mass yield rate of the polymeric precursor, i.e. the mass of ZnO produced per unit mass of resin, a certain mass of the resin (~6 g) was weighed and then annealed at 500 °C for 5 h. After this process, the final zinc oxide mass was determined. The resulting dry and brittle powder was ground and heat treated again for 12 h at 500 °C to enhance the elimination of any remaining organic compounds. Then, for the production of Yb$_x$Zn$_{1-x}$O NPs, stoichiometric amounts of Yb(NO$_3$)$_3$.5H$_2$O were dissolved in D-H$_2$O and added to the polymeric precursor, under magnetic stirring, until complete dissolution. The resulting solution was then annealed at 500 °C (for 5 h), ground, and heat-treated again at 500 °C for 12 h. Therefore, Yb$_x$Zn$_{1-x}$O NPs with variable Yb content (x) were produced. The diagram in Fig. 1 summarizes the whole process. The thermogravimetric analysis (TGA) and differential scanning calorimetry (DSC) was performed with a PerkinElmer STA8000. The measurements were made in the range of 30 to 900 °C, with a heating rate of 10 °C/min in N$_2$ flow. For the study of the structural properties of the as-produced nanoparticles, X-ray diffraction (XRD) measurements were made using

a diffractometer (D2-Phaser, Bruker) with CuKα radiation (λ$_m$=1.5418 Å). The experiments were carried out in the range of 20°≤2θ≤80°, with steps of 0.020° and a time per step of 0.25 s. The Rietveld method was implemented using EXPGUI-GSAS software [22, 23]. For the refinement, the standard corundum sample was measured. Fourier transform infrared spectroscopy (FTIR) was done using the KBr pellet method. For these studies, a spectrometer (Spectrum Two, PerkinElmer) was used.

RESULTS AND DISCUSSION

Pechini's method for the production of ZnO-based nanomaterials uses metal nitrates [such as Zn(NO$_3$)$_2$.6H$_2$O and Yb(NO$_3$)$_3$.5H$_2$O] as a source of cations, citric acid (CA) as a chelating agent, and ethylene glycol (EG) as an esterification agent [24]. Fig. 2 represents the chemical reaction expected for these reagents, which results in the polymeric precursor (resin). For a better understanding of the results obtained for the Yb$_x$Zn$_{1-x}$O NPs, the reagents and polymeric precursor were analyzed by thermogravimetric analysis (TGA) and differential scanning calorimetry (DSC).
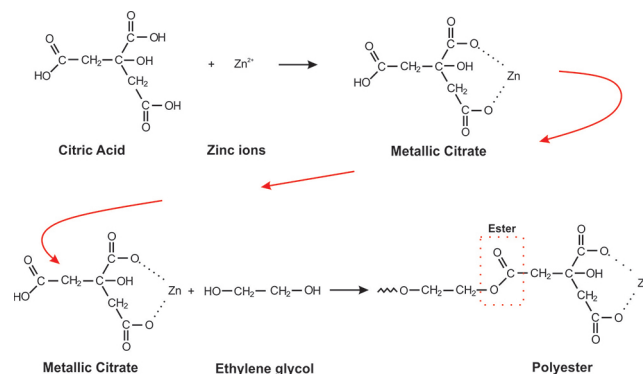
Figure 2: Schematic representation of the chemical reaction between citric acid, Zn^{2+} ions (from zinc nitrate hexahydrate), and ethylene glycol to produce the polymeric precursor (resin), which gives rise to ZnO NPs after thermal annealing.

TGA/DSC data of the as-produced resin and reagents (ethylene glycol, citric acid, and zinc nitrate hexahydrate) are shown in Fig. 3. These data show that the decomposition of the polymeric precursor occurred in some stages: room temperature (RT) to ~155 °C (i), ~155 to ~335 °C (ii), ~335 to ~490 °C (iii), and ~490 to 900 °C (iv). When comparing the first weight loss (i) with the decomposition of the reagents, it can be seen that this first step can be attributed mainly to the decomposition of excess ethylene glycol, zinc nitrate hexahydrate, as well as to the evaporation of the absorbed water [25]. In the second decomposition region (ii), characterized by the feature at ~275 °C, the decomposition and combustion of citric acid and nitrate molecules occurred, as suggested by Fig. 3b. In the third stage (iii), there was the decomposition and burning of residual carbon components, as well as the crystallization of ZnO. No pronounced weight loss was verified in the region (iv), which indicated the end of the thermal decomposition
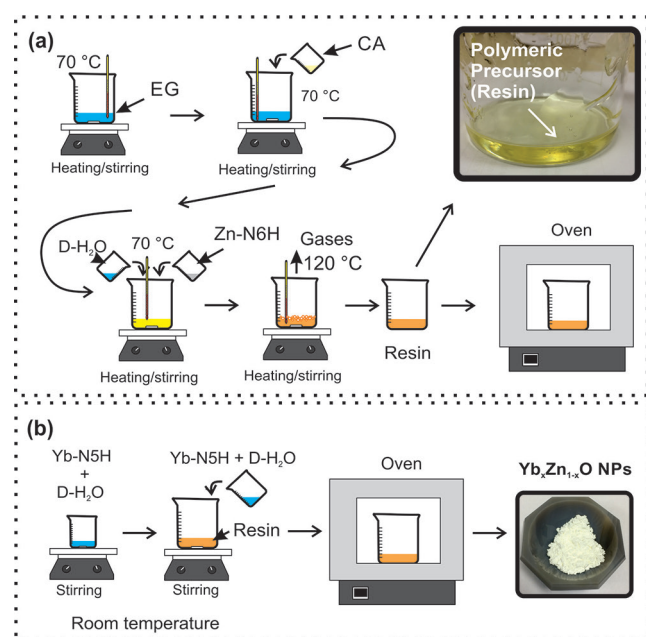

Figure 1: Schematic showing the production of the resin and ZnO nanoparticles from Pechini's method using ethylene glycol (EG), citric acid (CA), zinc nitrate hexahydrate (Zn-N6H), and deionized water (D-H$_2$O) (a), and representation of the synthesis of Yb$_x$Zn$_{1-x}$O NPs using ytterbium nitrate pentahydrate (Yb-N5H) (b).

of the polymeric precursor. Therefore, the TGA/DSC results suggested that the annealing temperature used (500 °C) was sufficient for the synthesis of $Yb_xZn_{1-x}O$ nanoparticles, with the elimination of most organics.
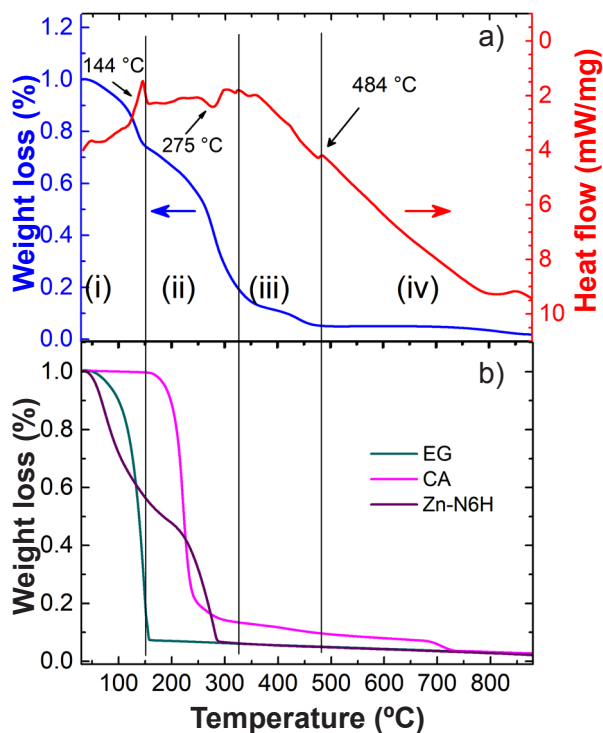

Figure 3: TGA and DSC curves of polymeric precursor with the indication of four decomposition stages: i, ii, iii, and iv (a), and TGA curves of ethylene glycol (EG), citric acid (CA), and zinc nitrate hexahydrate (Zn-N6H) (b).

In Fig. 4, FTIR spectra of the polymeric precursor and the $Yb_xZn_{1-x}O$ nanoparticles are shown. In the spectrum of the precursor, the broad band at $\sim$3450 cm^{-1} and the peak at $\sim$1635 cm^{-1} were due to the presence of hydroxyl groups (O-H) of water and derivatives of citric acid and ethylene glycol. The peak at $\sim$2950 cm^{-1} was attributed to the -CH$_2$ stretching vibrations [26]. For the same material, the band at $\sim$1730 cm^{-1} indicated the C=O stretching mode of ester, which is expected to be formed by the reaction between citric acid and ethylene glycol in the polymerization process (Fig. 2) [27]. It is important to note that these features (at $\sim$2950 and $\sim$1730 cm^{-1}) were not detected in the nanoparticle spectra. Evidence on the formation of zinc oxide was seen in all spectra of $Yb_xZn_{1-x}O$ NPs by the wide band at $\sim$450 cm^{-1}. This band was not present in the polymeric precursor spectrum and can be associated with the Zn-O stretching mode. For doped samples, the profile of this feature was distorted at $\sim$550 cm^{-1}, suggesting the presence of vibrations from the Yb-O bonds. Likewise, the small peak with Yb dependence at $\sim$850 cm^{-1} (superimposed on one observed for sample x=0.000 at $\sim$875 cm^{-1}) can also be credited to the vibration of the ytterbium-oxygen bond [28]. In addition to the bands related to Yb:ZnO NPs, other features can be identified. Among them, the absorption band centered at $\sim$3450 cm^{-1} and a small feature at $\sim$1635 cm^{-1} also can be attributed, respectively,

to the stretching and bending vibrations of O-H in H$_2$O. The peaks at $\sim$1395 and $\sim$1510 cm^{-1}, which exhibited increasing intensities with Yb^{3+} content, may be assigned to the symmetric and asymmetric stretching modes of the carboxyl group (C=O). Regarding the origin of this organic group and its dependence on Yb^{3+} content, organic groups can be adsorbed on the surface of the nanoparticles and interact with Yb^{3+}. As the ytterbium ions can accumulate on the surface of the nanoparticles, their presence can hinder the elimination of organics during the annealing process. The results presented in the following paragraphs are in accordance with this hypothesis.
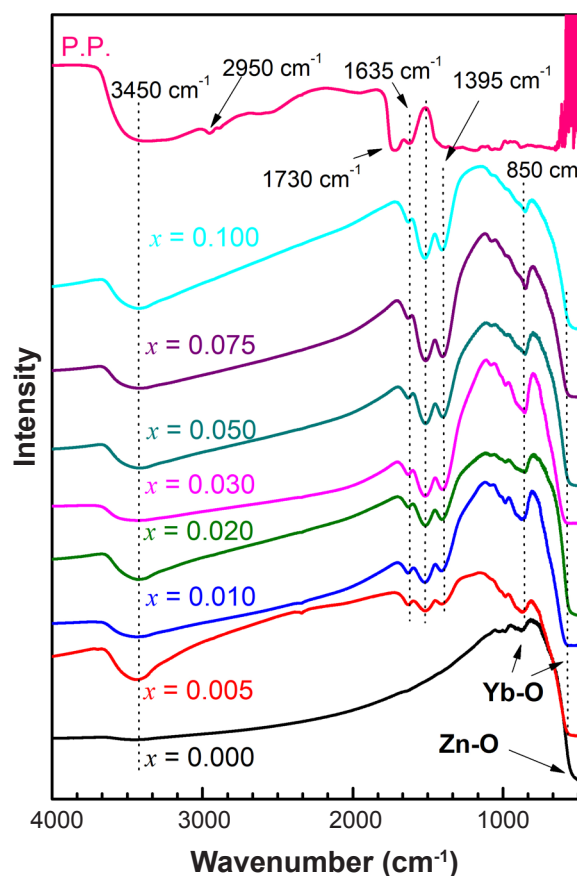

Figure 4: FTIR spectra of the polymeric precursor (P.P.) and $Yb_xZn_{1-x}O$ nanoparticles.

Fig. 5 shows the X-ray diffraction (XRD) patterns of the $Yb_xZn_{1-x}O$ nanopowders. Under typical conditions, zinc oxide-based materials crystallize in hexagonal wurtzite structure (space group P6$_3$mc), which presents zinc atoms arranged in a hexagonal close-packed symmetry. In Fig. 5, all the observed reflections are well indexed with the mentioned structure (JCPDS 79-2205). On the other hand, for samples with x=0.075 and 0.100, it was possible to identify small features marked with stars (*). These peaks were consistent with the presence of an impurity phase of cubic ytterbium oxide Yb_2O_3 (JCPDS 87-2374). This means that, for these two samples, the nominal Yb content in $Yb_xZn_{1-x}O$ NPs must be greater than the actual ytterbium concentration in the wurtzite structure due to Yb^{3+} segregation and formation of ytterbium oxide. It is also important

to point out that other synthesis routes, such as hydrothermal and combustion methods, can lead to the formation of ytterbium oxide in concentrations detectable by XRD for Yb content around 1% [14, 29, 30]. Regarding its physical properties, Yb_2O_3 has a high dielectric constant (~15), a large band gap (~5 eV), and exhibits antiferromagnetic non-collinear structure with a low Néel temperature of T_N=2.3 K [31, 32]. In fact, nanocomposites formed by ZnO/Yb_2O_3 also have applications for down-conversion due to the existence of energy transfer from ZnO to the Yb^{3+} ions [33, 34]. This possibility, however, is not explored here. Thus, the formation of an additional Yb_2O_3 phase can alter the optical, electrical, and magnetic properties of the samples.
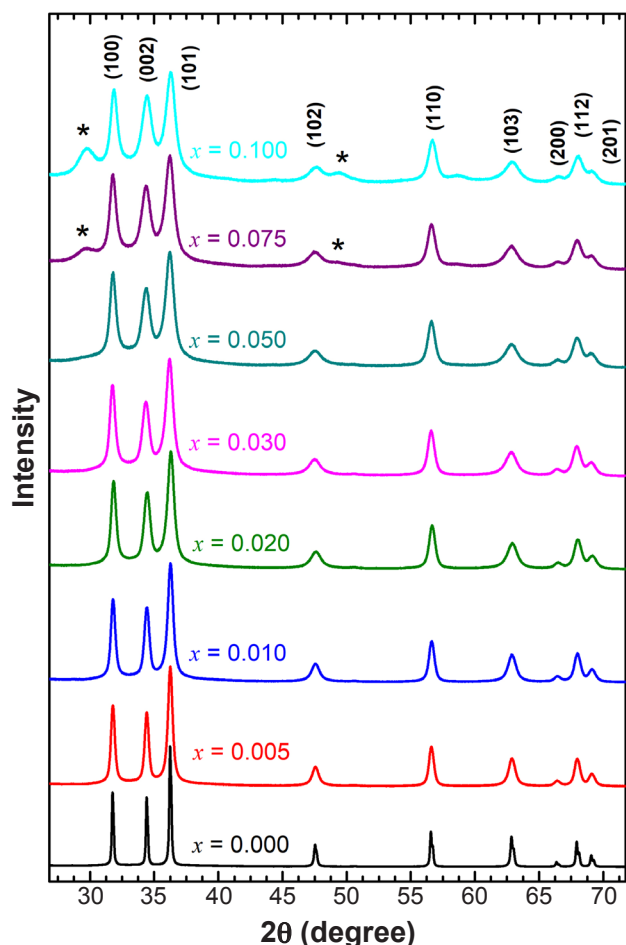

Figure 5: XRD patterns of the $Yb_xZn_{1-x}O$ nanoparticles ($0.000 \leq x \leq 0.100$). The stars (*) indicate peaks associated with Yb_2O_3.

In order to better understand the influence of Yb^{3+} on the wurtzite structure and to obtain more evidence on ytterbium doping, the XRD data were analyzed using the Rietveld method (RM). This method is a computational technique that combined with good XRD data can offer new possibilities for X-ray diffraction. In RM, the average particle size (L) can be found by the peak profile parameters, which take into account the Scherrer equation:

$$L = \frac{K.\lambda}{\beta.\cos\theta} \tag{A}$$

where K is the Scherrer constant (often adopted as 0.89, depending on particle shape), λ is the X-ray wavelength, and B is the width of the diffraction peak (corrected for instrumental broadening). In fact, in EXPGUI/GSAS software, the particle size can be obtained by the LX-parameter, which is used in the modified Scherrer equation: $L=18000K.\lambda/(\pi.LX)$. As can be seen in Table I, an abrupt decrease in the mean particle size from ~77 to 9.5 nm was observed as the Yb^{3+} content increased from 0.000 to 0.100 in $Yb_xZn_{1-x}O$ NPs. This behavior can be attributed to grain boundary pinning. In this process, the accumulation of Yb^{3+} on the surface of the nanoparticles hinders particle aggregation during synthesis [35]. Therefore, it is reasonable to think that there is a gradient of Yb content in the as-synthesized nanopowders, with its maximum on their surface. It can be noted that the average particle size reached values lower than those obtained by some other synthesis methods [20, 36, 37]. In addition, this result showed that RE doping can also be used as an alternative to control and reduce particle dimensions, which is a strategy to improve the physical properties of nanomaterials. Other results in the literature show constancy or even an increase in size with Yb doping [15, 20, 37].

By the use of XRD, it was observed that, while the a-lattice parameter changed slightly, the c-parameter tended to increase with Yb^{3+} content. In addition, the Rietveld method allowed the determination of the internal u-parameter (the length of the bond parallel to the c-axis [1]). It was observed that u increased almost linearly from 0.3924 to 0.4155, as shown in Table I. It is important to note that u deviated from the expected value for an ideal wurtzite structure, which is u=3/8=0.375. On the other hand, the cell volume showed an increasing trend with Yb^{3+} content, but with non-linear behavior. In order to better understand the dynamics of the crystalline structure with increasing Yb^{3+}, we can further explore the XRD/Rietveld data. Fig. 6 shows the representation of the crystalline structure of zinc oxide. In this wurtzite structure, the nearest-neighbor bond lengths along and off the c-direction, b and b_1, respectively, can be given by [1]:

$$b = c.u \tag{B}$$

$$b_1 = \sqrt{\frac{1}{3}\ a^2 + \left(\frac{1}{2} - u\right)^2 c^2} \tag{C}$$

On the other hand, the bond angles, α and β, are given by the following expressions:

$$\alpha = \frac{\pi}{2} + \arccos\left[\left(\sqrt{1+3\left(\frac{c}{a}\right)^2\left(-u+\frac{1}{2}\right)^2}\right)^{-1}\right] \tag{D}$$

$$\beta = 2\arcsin\left[\left(\sqrt{\frac{4}{3} + 4\ \left(\frac{c}{a}\right)^2\left(-u+\frac{1}{2}\right)^2}\right)^{-1}\right] \tag{E}$$

Since it is ideally expected that Yb^{3+} is introduced at a substitutional site of Zn^{2+} ions, this exchange should

Table I - Particle size, lattice parameters a and c (Å), cell internal parameter u, and unit cell volume (Å³) as a function of Yb^{3+} content.

Yb^{3+} content	Particle size (nm)	a (Å)	c (Å)	u	Cell volume (Å³)
0.000	76.7	3.250	5.206	0.392	47.63
0.005	24.3	3.249	5.208	0.396	47.63
0.010	20.0	3.250	5.210	0.394	47.65
0.020	17.6	3.250	5.211	0.397	47.65
0.030	14.7	3.249	5.213	0.397	47.66
0.050	11.7	3.249	5.213	0.402	47.65
0.075	10.7	3.248	5.213	0.409	47.65
0.100	9.5	3.250	5.215	0.416	47.70

produce crystalline cell deformation due to the increased size and valence of ytterbium. While Zn^{2+} has an ionic radius of around 0.74 Å, Yb^{3+} is much larger, with an ionic radius of 0.86 Å. Thus, the insertion of ytterbium into the wurtzite structure promotes crystalline deformations. In Figs. 6b and 6c, b, b_1, α, and β calculated from RM data are plotted. As a first consideration, it is possible to notice that all these parameters behaved linearly with Yb^{3+} content for all the x range, differently from a and c lattice parameters and cell volume. With these data, it is now possible to see the effect of doping. As shown by the parameters, as ytterbium content grew, the length of the bond along c-axis (b) increased, and the bond with extension given by b_1 diminished. In addition, the bond angles changed: as α decreased, β grew. Therefore, Yb^{3+} doping led to an average displacement of the central atom along the c-axis, although it did not show a clear trend in terms of cell volume or the behavior of parameters a

and c. Recently, López-Mena et al. [38], through the study of Yb-doped ZnO thin films produced by spin coating, demonstrated that ytterbium doping leads to a decrease of b_1. However, a clearer picture also including b, α, and β has not been reported so far. In addition, the results presented here reinforce that Yb^{3+} ions are introduced into the wurtzite structure, even for samples with x= 0.075 and 0.100, for which a secondary phase of Yb_2O_3 was detected by XRD. Thus, based on the results presented, we can argue that the calculation of b, b_1, α, and β is essential to understand the structural behavior caused by rare-earth doping. As shown, interpretations only about lattice parameters and cell volume are inconclusive to elucidate the behavior resulting from Yb^{3+} doping.

CONCLUSIONS

$Yb_xZn_{1-x}O$ nanoparticles, synthesized by the polymer precursor method, were successfully investigated by thermogravimetric analysis (TGA), differential scanning calorimetry (DSC), Fourier transform infrared spectroscopy (FTIR), and X-ray diffraction (XRD) for a wide doping range (0.000≤x≤0.100). TGA/DSC measurements of reagents and the polymeric precursor confirmed the crystallization of wurtzite nanoparticles (NPs) at a temperature below the annealing temperature (500 ºC). FTIR data showed the purity and good crystalline quality of the $Yb_xZn_{1-x}O$ NPs. A profile band distortion at around 550 cm^{-1} and a small FTIR peak with Yb dependence at ~847 cm^{-1} were interpreted as ytterbium-oxygen bond vibrations, which correlated well with the Yb^{3+} doping hypothesis. The XRD data also indicated the good crystalline quality of the samples. No evidence of phase segregation was observed for samples with x≤0.050. For the other samples, a Yb_2O_3 phase was detected. The Rietveld refinement method (RM) showed that the Yb^{3+} doping induced a reduction in the average particle size, with the lowest value (9.5 nm) achieved for the most doped sample. Additionally, although there was no clear trend for the growth of the unit cell volume and lattice parameters (a and c), the use of RM to calculate bond lengths (b and b_1) and angles (α and β) showed that the Yb^{3+} doping led to a linear
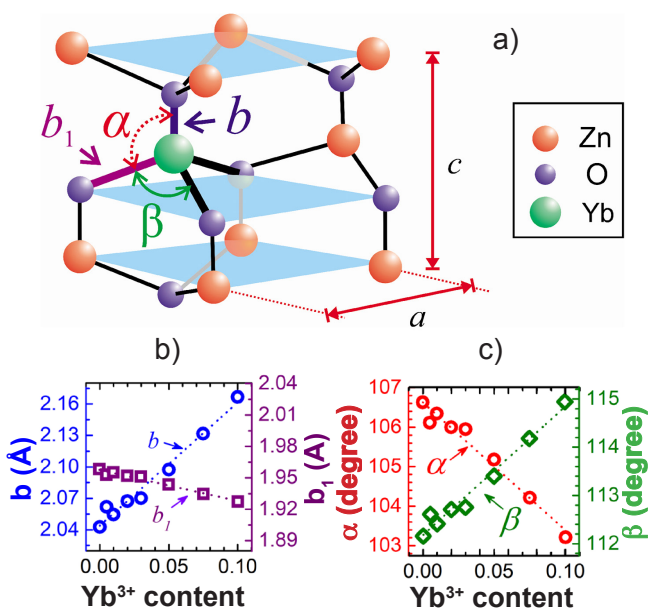

Figure 6: Representation of wurtzite structure (adapted from [1]) highlighting the bond lengths (b and b_1) and angles (α and β) (a), and values determined for b and b_1 (b), and α and β (c) as a function of Yb^{3+} content.

displacement of the central cation along c-axis. These data were interpreted as evidence of the insertion of Yb^{3+} in the wurtzite structure, which can indicate that Yb-doped ZnO NPs are promising materials for applications in spintronics, optoelectronics, dosimetry, photocatalysis, etc. Therefore, the results presented are in line with the effectiveness of the polymer precursor method for Yb^{3+} doping on zinc oxide, as well as the importance of employing the Rietveld method to determine crystalline dynamics.

ACKNOWLEDGMENTS

REFERENCES

[1] H. Morkoç, Ü. Özgür, *Zinc oxide: fundamentals, materials and device technology*, Wiley-VCH, Weinheim (2009) 490.

[2] D. Daksh, Y.K. Agrawal, Rev. Nanosci. Nanotechnol. **5**, 1 (2016) 1.

[3] M. Balestrieri, G. Ferblantier, S. Colis, G. Schmerber, C. Ulhaq-Bouillet, D. Muller, A. Slaoui, A. Dinia, Sol. Energy Mater. Sol. Cells **117** (2013) 363.

[4] V. Kumar, O.M. Ntwaeaborwa, T. Soga, V. Dutta, H.C. Swart, ACS Photonics **4**, 11 (2017) 2613.

[5] I. Soumahoro, G. Schmerber, A. Douayar, S. Colis, M. Abd-Lefdil, N. Hassanain, A. Berrada, D. Muller, A. Slaoui, H. Rinnert, A. Dinia, J. Appl. Phys. **109** (2010) 33708.

[6] U. Pal, R. Meléndrez, V. Chernov, M. Barboza-Flores, Appl. Phys. Lett. **89**, 18 (2006) 183118.

[7] E. Guziewicz, R. Ratajczak, M. Stachowicz, D. Snigurenko, T.A. Krajewski, C. Mieszczynski, K. Manzur, B.S. Witkowski, P. Dluzewski, K. Morawiec, A. Turos, Thin Solid Films **643**, 1 (2017) 7.

[8] Y. Liu, C. Xu, Q. Yang, J. Appl. Phys. **105** (2009) 84701.

[9] S.S. Syamchand, R.S. Aparna, G. Sony, Microchim. Acta **184** (2017) 2255.

[10] C.L. Heng, W. Xiang, W.Y. Su, H.C. Wu, Y.K. Gao, P.G. Yin, T.G. Finstad, Opt. Mater. Express **7**, 8 (2017) 3041.

[11] Y. Liu, Q. Yang, C. Xu, J. Appl. Phys. **104** (2008) 64701.

[12] M. Lluscà, J. López-Vidrier, A. Antony, S. Hernández, B. Garrido, J. Bertomeu, Thin Solid Films **562**, 1 (2014) 456.

[13] A. Balakrishna, T.K. Pathak, E. Coetsee-Hugo, V. Kumar, R.E. Kroon, O.M. Ntwaeaborwa, H.C. Swart, Colloids Surf. A **540**, 5 (2018) 123.

[14] E. Cerrato, G.A. Zickler, M.C. Paganini, J. Alloys Compd. **816**, 5 (2020) 152555.

[15] Q. Yin, X. Jin, G. Yang, C. Jiang, Z. Song, G. Sun, RSC Adv. **4** (2014) 53561.

[16] Y. Al-Hadeethi, A. Umar, K. Singh, A.A. Ibrahim, S.H. Al-Heniti, B.M. Raffah, J. Nanosci. Nanotechnol. **19**, 7 (2019) 4199.

[17] S.M.C. Miranda, M. Peres, T. Monteiro, E. Alves, H.D. Sun, T. Geruschke, R. Vianden, K. Lorenz, Opt. Mater. **33**, 7 (2011) 1139.

[18] W. Jia, K. Monge, F. Fernandez, Opt. Mater. **23**, 1-2 (2003) 27.

[19] H. Li, Z. Zhang, J. Huang, R. Liu, Q. Wang, J. Alloys Compd. **550**, 15 (2013) 526.

[20] D.K. Sharma, M. Varshney, S. Shukla, K.K. Sharma, V. Kumar, A. Sharma, Vacuum **179** (2020) 109522.

[21] F.H. Aragón, J.A.H. Coaquira, P. Hidalgo, R. Cohen, L.C.C.M. Nagamine, S.W. da Silva, P.C. Morais, H.F. Brito, J. Nanopart. Res. **15** (2013) 1343.

[22] A.C. Larson, R.B. Von Dreele, "General structure analysis system (GSAS)", Los Alamos Nat. Lab. Report LAUR 86-748 (1994).

[23] B.H. Toby, J. Appl. Cryst. **34** (2001) 210.

[24] S. Bachir, K. Azuma, J. Kossanyi, P. Valat, J.C. Ronfard-Haret, J. Lumin. **75**, 1 (1997) 35.

[25] Z.N. Kayani R. Ishaque, B. Zulfiqar, S. Riaz, S. Naseem, Opt. Quant. Electron. **49** (2017) 223.

[26] E.E.J. Mary, K.S. Suganthi, S. Manikandan, N. Anusha, K.S. Rajan, J. Taiwan Inst. Chem. Eng. **49** (2015) 183.

[27] S. Qiu, H. Fan, X. Zheng, J. Sol-Gel Sci. Technol. **42** (2007) 21.

[28] A. Umar, A.A. Abrahim, R. Kumar, T. Almas, M.S. Al-Assiri, S. Baskoutas, Ceram. Int. **45**, 11 (2019) 13825.

[29] M. Achehboune, M. Khenfouch, I. Boukhoubza, B. Mothudi, I. Zorkani, A. Jorio, J. Phys. Conf. Ser. **1292** (2019) 12021.

[30] V. Kumar, A. Pandey, S.K. Swami, O.M. Ntwaeaborwa, H.C. Swart, V. Dutta, J. Alloys Compd. **766** (2018) 429.

[31] T.M. Pan, W.S. Huang, Appl. Surf. Sci. **255**, 9 (2009) 4979.

[32] R.M. Moon, W.C. Koehler, H.R. Child, L.J. Raubenheimer, Phys. Rev. **176** (1968) 722.

[33] M.V. Shestakov, A.N. Baranov, V.K. Tikhomirov, Y.V. Zubavichus, A.S. Kuznetsov, A.A. Veligzhanin, A.Y. Kharin, R. Rösslhuber, V.Y. Timoshenko, V.V. Moshchalkov, RSC Adv. **2** (2012) 8783.

[34] O.A. Shalygina, I.V. Nazarov, A.V. Baranov, V.Y. Timoshenko, J. Sol-Gel Sci. Technol. **81** (2017) 333.

[35] N.C. Sena, T.J. Castro, V.K. Garg, A.C. Oliveira, P.C. Morais, S.W. da Silva, Ceram. Int. **43**, 5 (2017) 4042.

[36] I. Ahmad, Sep. Purif. Technol. **227** (2019) 115726.

[37] S.D. Senol, J. Mater. Sci. Mater. Electron. **27** (2016) 7767.

[38] E.R. López-Mena, O. Ceballos-Sanchez, T.J.N. Hooper, G. Sanchez-Ante, M. Rodríguez-Muñoz, J.A. Renteria-Salcedo, A. Elías-Zuñiga, A. Sanchez-Martinez, J. Mater. Sci. Mater. Electron. **32** (2021) 347.

(Rec. 21/10/2020, Rev. 04/02/2021, Ac. 01/03/2021)